Vrije Universiteit Amsterdam

Universiteit van Amsterdam

Master Thesis

RALEF-2D for Modeling Laser-Produced Plasma: Investigating Anisotropy in Plasma Expansion for Varying Laser Intensities

---

Author: Mardou Bijker   (113409980)

1st supervisor: dr. John Sheil
daily supervisor: Diko Hemminga   (ARCNL)
2nd reader: dr. Oscar Versolato

A thesis submitted in fulfillment of the requirements for
the joint UvA-VU Master of Science degree in Physics and Astronomy

July 17, 2023

Abstract

In this work, the RALEF-2D code is used to simulate tin laser-produced plasma expansion into vacuum using a single-fluid, single-temperature approach. A 27 μm tin droplet is irradiated by a Nd:YAG ($\lambda = 1.064$ μm) laser with laser energies varying between $5 - 100$ mJ. We study the movement in which the plasma expands and the changes for different laser energies. The results from the simulations are compared with previously obtained experimental results. Doing simulations can provide a better understanding of the changes that show in the ion energy distributions - when varying laser energy - in the experimental results. Thus, understand the LPP expansion better. Simulations are compared with experiments and are in good agreement. We find that the high-energy peak in the ion energy distributions is reproduced in the simulations. We find a power-law relation between the peak position and the laser intensity, that matches experiments and is related to theory. This gives the promising result that RALEF shows predictive powers to LPP expansion.

Contents

List of Figures

1

Introduction

Generating extreme ultraviolet (EUV) light is the key ingredient in making the smallest and fastest computer chips at present using nanolithography technology. For these lithography machines to produce chips on nanoscale, EUV light with a wavelength of 13.5 nm is needed. We zoom in on the source of this EUV light, which is tin Laser-Produced Plasma (LPP). An LPP is created by a laser beam irradiating a solid or liquid target. The laser illuminating the target ionizes the atoms, allowing electrons to move at high velocities in the plasma. When electrons collide with ions and recombine, light will be emitted from the plasma. The light we are interested in is the 'In-band' emission from the tin LPP, which shows spectra near this EUV wavelength (13.5 ± 0.135 nm). The EUV light is collected and focussed to be transmitted further in the machine.
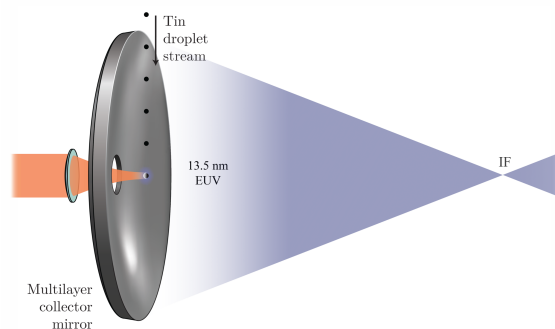
Figure 1.1: Schematic drawing of the setup. The laser is incident of a tin microdroplet from the left. The molybdenum/silicon multilayer collector mirrors reflect and focus the emitted EUV light at the intermediate focus (IF). This figure is reproduced from Ref [1].

In this thesis, we take a theoretical approach by simulating tin LPP expan-

sions. We consider four cases where the LPP is generated by four different laser energies that are also studied experimentally. In these experiments, EUV light is emitted from tin LPP, as mentioned above. As is shown in Fig 1.1, molybdenum/silicon multilayer mirrors (MLM) are placed around the droplets to reflect and focus the EUV light to be transmitted further in the machine and be used in the lithography process. The MLM have a light reflection of 70% for the in-band region ($\lambda = 13.5$ nm $\pm 1\%$) [6]. However, EUV light is not the only emission from the droplet. Upon the incident of the laser on the tin droplet, the LPP expands and emits ions in all directions. These ions could potentially damage the sensitive optics in the EUV machines and thus reduce the EUV throughput. One can place a strong magnetic field around the target to stop the ions from flying off to the mirrors [7, 8, 9]. Another way to protect the MLM is adding background hydrogen around the mirrors to stop the ions from reaching and harming them [8, 10, 11]. The goal of this thesis is to understand the expansion of tin LPP when illuminated by an Nd:YAG laser ($\lambda = 1.064$ μm) with intensities varying between $0.4 - 8 \cdot 10^{11}$ W/cm^2. By knowing the direction whereto the plasma emits ions and what kinetic energy these ions carry, we can better protect the surrounding optic. Ion energy distributions - quantifying the number of ions with a certain energy - are experimentally obtained at 7 angles around the target for varying laser pulse energies. Simulations have been done for one of those laser pulse energies, but not for varying laser energies.

1.1 Models Used for Simulating LPP Expansion

Tin plasma expansions have been studied and reproduced by simulations before. Murakami *et al* [4] and Fujioka *et al* [12] recorded ion energy distributions for minimum-mass targets being illuminated by a 10-ns laser pulse (of the same Nd:YAG laser that we use), describing the expansion as an isothermal plasma expansion. Shorter laser pulses (ps duration pulse) have been researched as well and their ion energy distributions are better described by a planar isothermal expansion model described by Mora *et al* [2]. These models are both analytical models, meaning that they need to make simplifying assumptions to create input for the models. They assume that the shape of the laser does not influence the plasma expansion, thus treating the plasma as if it is uniformly

heated before the expansion starts. Because those models acquire a set density profile. Murakami *et al* uses a Gaussian density profile and Mora's model an exponential one. The different density profiles used in the models influence the ion energy distributions significantly as is shown in Hemminga *et al* [5]. In this thesis we use a numerical model named RALEF-2D (Radiation Arbitrary Lagrangian-Eulerian Fluid dynamics). This model includes radiation emitted from the plasma and more importantly, generates a density profile function $\phi(d/t)$ at each moment in time during the expansion. This is a much more complex calculation and requires a lot of computational power. Now one can simulate the 3D target being hit by a laser and present it with a 2D simulation and simulate it as a radiating (non-planar), non-uniformly heated plasma expansion.

1.1.1 RALEF-2D

For our case of the expanding tin LPP, Marakami and Mora's models obtain ion energy distributions that are not in good agreement with the experiments. This is because the expanding tin LPP deals with a lot of energy converting into radiation, which is not included in those models. This is where RALEF-2D steps in. RALEF-2D is a numeric two-dimensional radiation-hydrodynamic model that treats the expanding plasma as a fluid, using a single-temperature and single-fluid approach. The workings of the RALEF-2D code to describe the expansion of the tin LPP expansion will be discussed in greater detail in Ch. 2.

In this thesis, we simulate the tin LPP expansion using the RALEF-2D model. We check whether RALEF obtains the same ion energy distributions ($dN^2/dEd\Omega$) and angular distributions as the experiments that have been done for varying laser-pulse energies. This has two main purposes. First, by doing simulations of the expansion we can observe how the simulated fluid behaves while expanding and thus understand the experimental results better. The latter can help understand and explain observations in the $dN^2/dEd\Omega$ distributions, such as why there is there a peak in the ion energy distribution at high energy as is explained for the 60°emission angle in [5]. The second reason for testing the model is to check whether the model holds, not only for a single laser pulse case as is done in [13], but also for multiple laser pulse energies at varying

emission angles. If this would be the case and RALEF can simulate the LPP expansion for all these different cases, one could conclude that it describes the plasma expansion and ion emission accurately. Continuing, one could - by doing simulations - make predictions of the ion energy distributions for all emission angles. This way radiation-hydrodynamic model can then be used to predict plasma expansions and the accessory ion emissions when hitting tin droplets with arbitrary laser energy.

2

Theory and Simulations

In this chapter, we provide background and theory on generating laser-produced plasmas (LPPs). Since running LPP experiments is cumbersome and requires expensive equipment, we are interested in modeling this process, specifically focusing on tin LPP and the subsequent plasma expansion. After introducing the necessary theory, we argue why a fluid approach is a justifiable model for plasma expansion. Next, we introduce the single-fluid, single-temperature approximation that we use in our simulations, and explain why this approach can be faithfully applied to the cases we study in this thesis. RALEF-2D's fluid equations use. To finally quantify plasma expansions, the distributions of particles over their kinetic energies are a way, which is the main result end which we will explain in chapter 3.

2.1 LPP Theory

A plasma can be described as an ionized gas, where positively charged ions, negatively charged electrons, and neutral atoms are all mixed. In a gas, however, electrons do not have long-range electromagnetic interactions, whereas, in plasma long-range interactions do exist. As a result of these long-range interactions, there are collective motions of the ions, atoms, and electrons in the plasma. In this thesis, we are interested in tracking this collective motion of a tin laser-produced plasma (LPP), to accurately describe the direction in which the plasma expands. An LPP is created by irradiating a solid or liquid target

with a laser beam, which heats and ablates the material into a plasma. The laser beam typically has an intensity of 10^8 - 10^{21} W/cm^{-2} [14, 15].

2.1.1 LPP used for generating EUV light

To obtain LPP that radiates EUV light, the range of suitable laser intensities slims drastically to 10^9 - 10^{12} W/cm^{-2}. The laser irradiates the tin droplets and ionizes the tin atoms. The electrons in the tin atoms absorb the laser light and when emitting from the atoms, move around at high velocities, thus rapidly increasing the electron temperature T_e, this process is called inverse Bremmstralung. When the electrons move fast in the LPP, they can recombine with the tin ions, which causes light to be emitted again. Different ions typically have different recombination energies. What makes tin such a good EUV source is that all Sn^{11+} - Sn^{15+} ions have the atomic configuration to emit in the in-band region of $\lambda = 13.5 \pm 0.135$ nm light [16, 17, 18, 19, 20]. This in-band light is collected by the multilayered mirrors with high reflectivity, as mentioned before.

An LPP used for generating EUV light to be used in nanolithography technologies is considered to be quasineutral, thus the electron number density n_e is related to the ion number density n_{ion} by

$$n_e = Zn_{ion}, \tag{2.1}$$

with Z being the average charge state of plasma. Furthermore, quasi-neutrality means that the overall charge of a material is neutral. Of course, at miniature scales, this assumption does not hold, because of differences in charge between ions and surrounding electrons, but this can be neglected at the scale that we are modeling. A good check on whether a plasma with electron temperature T_e and a density n is to be treated as neutral is with the use of the Knudsen number $K_n = \lambda/L$. The dimensionless Knudsen number describes the ratio of the mean free path of an electron λ (cm) $= 744\frac{T_e^2 \text{ (K)}}{n_e \text{ (cm)}^{-3}}$ to the total length scale of the system (the plasma gradient) $L = \frac{n}{|\nabla n|}$ [21]. For a fluid to be considered neutral, the Knudsen number must be small ($K_n \ll 1$) and the Debye length $\lambda_D = [T_e/ (4\pi n_e e^2)]^{1/2}$ much shorter than the plasma gradient L. These conditions are often met in hot and dense plasmas, so the LPP is considered quasineutral.

2.1.2 Speed of Sound in a Plasma

In this section we derive the equation for the speed of sound in a plasma, which we use to derive the sonic speed energy in the following section. Furthermore, we look at the sonic speed energy and the relation that is found between the sonic speed energy and a laser intensity illuminating a tin LPP [22]. This is of interest because we are interested in the speed of ions in a plasma - simulated as a fluid. We can study and compare whether the speed of sound and the speed of the fluid vary similarly with the laser intensity.

From Newton's second law, $F = ma$, the speed at which a sound wave propagates in an elastic medium can be derived. For simplicity, we consider a 1D scenario. The derivation of the speed of sound from Newton's second law goes as follows

$$a = \frac{F}{m}, \tag{2.2}$$

$$\frac{dv_{sw}}{dt} = -\frac{1}{\rho}\frac{dz}{dt}, \tag{2.3}$$

$$\rho\frac{dv_{sw}}{dt}\frac{dz}{dt} = -\frac{p}{dz}\frac{dz}{dt}, \tag{2.4}$$

$$-v_{sw}^2\frac{d\rho}{dt} = -\frac{p}{dt} = -\frac{dp}{d\rho}\frac{d\rho}{dt}, \tag{2.5}$$

$$c_s = v_{sw} = \sqrt{\left(\frac{dp}{d\rho}\right)_s}. \tag{2.6}$$

The movement is caused by the pressure difference, where the pressure and density in the wave are larger than its surroundings. Using the ideal gas equations

$$pV = Nk_BT, \text{ or} \tag{2.7}$$

$$p = nk_BT = \frac{\rho}{m_{ion}}k_BT, \tag{2.8}$$

we find that the speed of sound for isothermal processes (heat transfer during the expansion process, and $T = C$) is

$$c_{s,\text{ isothermal}} = \sqrt{\frac{k_BT}{m}}. \tag{2.9}$$

In the LPP, both the adiabatic and the isothermal speed of sound need to be taken into account. For simplicity, the isothermal sound speed is considered.

The pressure in the plasma is a sum of the pressure of the ions and the pressure of the electrons, $p = p_{ions} + p_e$. Assuming a single-temperature approach, $T = T_e = T_{ion}$, and we have a quasineutral (Eq. 2.1), highly ionized ($Z \gg 1$) plasma we can write (with Eq. ??) that the pressure in the plasma reduces to

$$p = p_i + p_e = n_i k_B T_i + n_e k_B T_e = k_B T(ni + n_e) = k_B T(n_i + Z n_i)$$
$$= n_i k_B T(1 + Z) \approx Z n_i k_B T = Z \frac{\rho}{m_i} k_B T. \tag{2.10}$$

Filling in the obtained pressure in 2.6 gives us a speed of sound in the plasma which then reads

$$c_{s, \text{ plasma}} = \sqrt{\left(\frac{dp}{d\rho}\right)_s} = \sqrt{Z} c_s. \tag{2.11}$$

The sound speed is a good metric to compare the velocities of moving ions in the plasma.

2.1.3 Sonic Speed Energy Relation to Laser Intensity

With $E_{\text{s}} = \frac{1}{2} m c_s^2$ we can translate the sound speed to sonic speed energy. The sonic speed energy of the plasma has been found to have a relation with the local temperature in the plasma [2, 4]

$$E \propto zT, \tag{2.12}$$

where z is the charge state. Basko *et al.* [22] found that the average charge state ($\bar{z}$) in a tin LPP scales with the local temperature T with a power law as

$$\bar{z} \propto T^{0.6}. \tag{2.13}$$

They also found that the local temperature scales with the laser intensity as

$$T \propto I^{0.44}. \tag{2.14}$$

Combining equations 2.12, 2.13 and 2.14 gives us a relation between the sonic speed energy and the intensity of the laser. The prediction of the position of the energy reads

$$E \propto T \cdot T^{0.6} \propto \left(I^{0.44}\right)^{1.6}$$
$$E \propto I^{0.70}. \tag{2.15}$$

Although the ions in the plasma do not move at sonic speed, the ions' movement is likely also influenced by the illuminating laser. Conceivably a similar relation between the ion's kinetic energy and the laser pulse energy could be captured.

2.2 LPP Simulation Models

We first describe a number of existing analytical approaches to modeling LPP expansions and experimentally show that their simplifying assumptions lead to derivations that do not match experimental spectra. Instead, we focus on a numerical simulation model, which allows for a more detailed approximation of the plasma expansion.

2.2.1 Limitations of Analytical Simulation Models

In this section, we discuss two analytical models that are used to describe plasma expansions based on some simplifications of the process. Both require a density profile and a pressure gradient in their model. As briefly described in the introduction, Murakami *et al.* [4] and Mora *et. al* [2] describe simple analytical models for hydrodynamic expansion of LPPs, with a Gaussian and exponential density profile respectively. Murakami *et. al* uses a single-fluid approximation with a quasi-isothermal approach while the laser irradiates the target, followed by a quasi-adiabatic approach when the laser is turned off.
The models can capture a 1D expansion from a 2D target, but for a 3D target - such as the droplet target in this thesis - they do not show a peak in the high-energy region that is observed in the experiments. Both models also do not take into account the heating of the fluid by the laser and make harsh assumptions describing specific density profiles, resulting in unrealistic results of the ion energy distributions. In Fig 2.1, reproduced from Hemminga *et al.*, we presented the ion energy distributions obtained by a planar isentropic (adiabatic and reversible) expansion (better known as the Riemann wave [3]), Mora, Murakami and the RALEF-2D model and compare these to an experimentally obtained distribution. None of the presented models, except for RALEF, show an increase in dN/dE at higher energy, which is present in the experimentally obtained $dN^2/dEd\Omega$. The RALEF simulation does show a peak and also corresponds better with the near-constant behavior for $E < 2keV$.

2.2.2 Alternative Models to Simulate a fluid

There are more methods studied to model a plasma expansion as a fluid expansion. When a fluid is considered non-neutral (not in LTE) the particle-in-cell
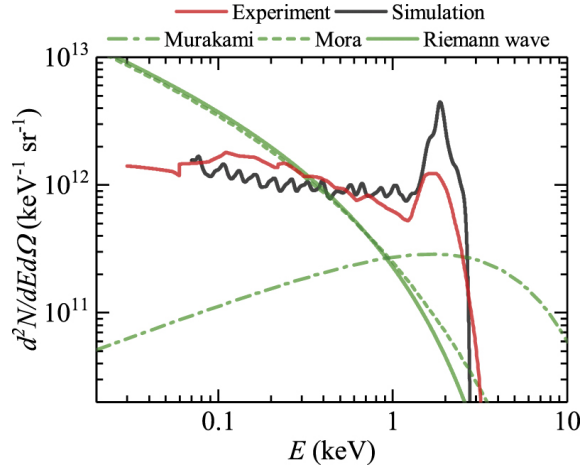
Figure 2.1: Ion energy distributions obtained by experiments (red solid), the planar isothermal expansion model of Mora (green dashed) [2], the Riemann wave (green solid)[3], Murakami (green dash-dot) [4] and the numerical RALEF-2D model (black solid line). This figure is obtained from [5].

(PIC) method can be used [23]. This method looks at all ions and electrons in an area and tracks each of their movements separately. This method requires a lot of computational power and time and for the hot and dense plasma we study there are too many ions, atoms and electrons to track individually and these calculations would be very hard to solve.

Other, also advanced, approaches to module fluid movements are the two-fluid, two-temperature approach where the ions and electrons are treated as two fluids with both their own temperatures [24], or a single-fluid, two-temperature approach [25]. In the following section, we argue why these approaches are not necessary for the description of the plasma expansion we study in this thesis and that a more simplified single-fluid, single-temperature approach - which RALEF uses - suffices.

2.2.3 Single-Fluid, Single-Temperature Approach

The radiation-hydrodynamic model, which we use to do simulations, models the plasma expansion as a fluid. To simplify the system, a single-fluid, single-temperature approach is assumed to model the formation of the LPP and the expansion that follows.

The single-temperature assumption means that the temperature of the ions and the electrons in the fluid are considered to be equal $T = T_{ion} = T_e$. Studies by

Sunahara and Tanaka [25] have simulated Nd:YAG lasers irradiating lithium, plastic and gold, and found that the ion temperature T_{ion} and the electron temperature T_e differ less than 20%, validating the single-temperature approach. The electrons move faster and much more easily than the ions and also absorb laser irradiation - giving the electrons a lot of kinetic energy. With the electrons flying around with high kinetic energies, they cause a lot of collisions with ions. During each of these collisions, a part of the kinetic energy is transmitted from the electrons toward slowly heating the ions. The fluid temperature thus depends on the electron temperature T_e. When the ion temperature and the electron temperature locally are the same $T_{ion} = T_e$, the plasma is in local thermal equilibrium (LTE).

A single-fluid model assumes that there are no individual ions, atoms and electrons in the fluid, but that these are all treated as the same. This is an approximation built on that the plasma is assumed to be quasineutral. Because the mass ratio of the tin ion and an electron $m_{Sn}/m_e \approx 10^5$, the fluid density is determined by the mass of the tin ions.

With the temperature of the plasma being dominated by only the electron temperature T_e and the fluid density being dominated by the mass of the tin ions, the single-fluid, single-temperature suffices.

2.3   RALEF-2D Simulation Properties and Output

In this section we discuss the working of the RALEF-2D code. With the RALEF-2D we have done radiation-hydrodynamic simulations of expanding plasma. The hydrodynamics part in RALEF-2D is based on an upgraded version of the 2D ideal hydrodynamics model CEVEAT [26]. The model has shown to be useful in simulating LPP expansions in previous research [27, 28, 29]. The way RALEF generates its results will be discussed and the inputs for the simulations that are done in this thesis are presented.

The radiation-hydrodynamic model numerically solves the hydrodynamic differential equations obtained for a single-fluid, single-temperature approach which read

$$\frac{\partial \rho}{\partial t} + \nabla \cdot (\rho \mathbf{v}) = 0 \tag{2.16}$$

$$\frac{\partial \rho \mathbf{v}}{\partial t} + \nabla \cdot (\rho \mathbf{v} \otimes \mathbf{v}) + \nabla \cdot p = 0 \tag{2.17}$$

$$\frac{\partial \rho E}{\partial t} + \nabla \cdot \left((\rho E + p) \, \mathbf{v} \right) - (S_T + S_R + S_{ext}) = 0. \qquad (2.18)$$

Because RALEF is a numerical model, it describes the expansion by solving the hydrodynamic equations including radiation (Eq. 2.16, 2.17 & 2.18) for each time iteration - taking into account that the modeled fluid absorbs and emits light -. The solutions are given in two spacial dimensions using a second-order Godunov-type method [29]. These solutions are displayed on an adaptive quadrilateral mesh with Cartesian (x,y) or axisymmetric (z,r) coordinates. The latter coordinate system is used in this thesis. A simplified example of the mesh is presented in Fig 2.2.

What sets RALEF apart form the previously discussed models is that it does
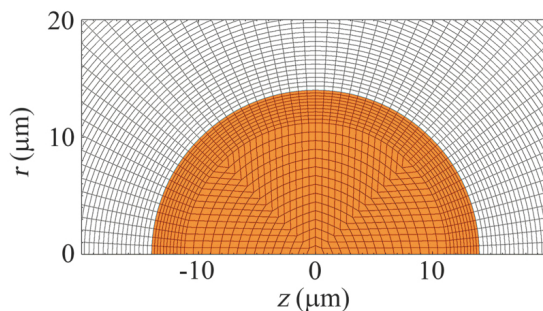
Figure 2.2: Schematic example of the axisymmetric mesh that RALEF-2D uses. The 27μm tin droplet is presented in orange. The area surrounding the droplet is filled with a background Sn vapor with a mass density of 10^{-12} g cm^{-3}. This figure is reproduced from Ref [5].

not need to make as many assumptions as the analytical models. More complex computations are done to find solutions to the hydrodynamic equations. The heating of the fluid by the laser is included, as well as the influence of the shape of the laser. This enables the model to generate a density profile function $\phi(d/t)$ at each moment in time during the expansion.

RALEF can also include the refraction of the incoming laser light, causing the light to slightly bend at the plasma surface. For this thesis, we do not include this function of the code and assume no refraction.

The goal of running the simulations is to be able to check whether we can reproduce experiments and compare results with the experimentally obtained results. This is why the experimental laser-droplet parameters serve as input to the simulations. We enter four laser energies between $5 - 100$ mJ that have been experimentally studied [13]. The Nd:YAG ($labmda = 1.064 \ \mu$m) laser has

a Gaussian profile with a special full-width half maximum $\text{FWHM}_{xy} = 100\ \mu\text{m}$ and a temporal full-width half maximum $\text{FWHM}_t = 10$ ns is implemented in the model. The laser pulse has a total pulse time of 30 ns. In order to match the experiments we give input energies $E_L = 5, 25, 58$ and 97 mJ, which with $I = (2\sqrt{2ln(2)/2\pi})^3 * E_L/FWHM_{xy}^2 FWHM_t$ translate to laser intensities between $I = 0.4 - 0.40 \cdot 10^{10}$ W/cm^{-2}. The 27 μm droplet is placed in the center of the mesh - as presented in Fig 2.2 - and a background Sn vapor with a mass density of 10^{-12} g cm^{-3} is added throughout the rest of the mesh.

3

Results and Discussion

In this chapter, we present and discuss the obtained results from the previously described RALEF-2D simulations. The hydrodynamics code enables us to have a detailed look inside the plasma expansion, which can help us describe and understand the process better. First, we will show and compare 2D visualizations of the speed and density of the LPP expansion after being hit by low and high laser energy, 8 mJ and 97 mJ. This is an interesting view, as it is not possible to track these properties during the expansion when doing experiments. Next, 1D profiles of the speed and density of the plasma are shown along several emission angles taken from 2D plots. This enables a better understanding of the observations one can make in the 2D plots. Different laser pulse energies varying between 5 and 100 mJ, emission angles, and moments in time are being compared and presented in these 'lineouts'. Following the 1D profiles, ion energy distributions of seven emission angles resulting from the simulations are presented and compared to earlier experimentally obtained results. Next, we discuss the high-energy-peak position shown in the recorded ion energy distributions and find a relation to laser intensity. Finally, the anisotropic behavior of the emission is shown. For the four laser energies, angular distributions of the total number of ions (obtained from the density profiles), the total energy, and the momentum of the ions are presented.

3.1 Two-Dimensional Visualisation of Expanding LPP

In this section, we present the expanding LPP at six moments in time after the tin droplet gets illuminated by a laser pulse energy (E_L) of $E_L = 8$ mJ and $E_L = 97$ mJ. The 2D profiles enable us to observe the behavior of the LPP during the expansion, which offers a deeper understanding of the final results in the experiments. In Fig 3.1 and 3.2 two of the four analyzed laser intensities are shown.

The figures show the expansion of the tin LPP at different times after illumination of the 8 mJ and 97 mJ laser beams respectively. The laser approaches the droplet from the left in a straight line at $z = 0$ for a duration of 30 ns. In each graph in the figure, the top half presents the velocity of the material and the bottom half presents the density of the tin plasma. Due to the Gaussian shape of the laser pulse, at t = 15 ns the intensity is at its maximum and thus also the temperature in the expanding plasma is at its maximum [5]. Around this time a 'second burst' of velocity appears, as can be seen in the figure. This is a result of the Gaussian Laser Pulse shape. As the pulse first reaches the target, the intensity is not yet at its maximum. However, the droplet keeps heating up from the laser hitting the droplet. Later, as the intensity builds up to its maximum, the droplet is heating up, causing the pressure to rise. With the pressure rising at the droplet surface, the pressure difference then results in the hot and dense plasma moving outwards, following from Eq. 2.17. The latter is visible from the 15 ns panel, and later panels, where a second burst of velocity shows. As the plasma, close to the initial tin droplet, then moves out faster than the less heated, slower moving plasma which started emitting earlier, it is creating a dense area. This is visible in the lower half of the panels 15-65 ns, there is an area with a higher density in the lower half of each panel. As time evolves in those panels, the second burst catches up (and eventually blends in) with the first velocity burst. Over this time, in the bottom half of the panels, it can be seen that there is a higher density area at a radial distance just further than the radial distance of the second velocity burst, as mentioned above.
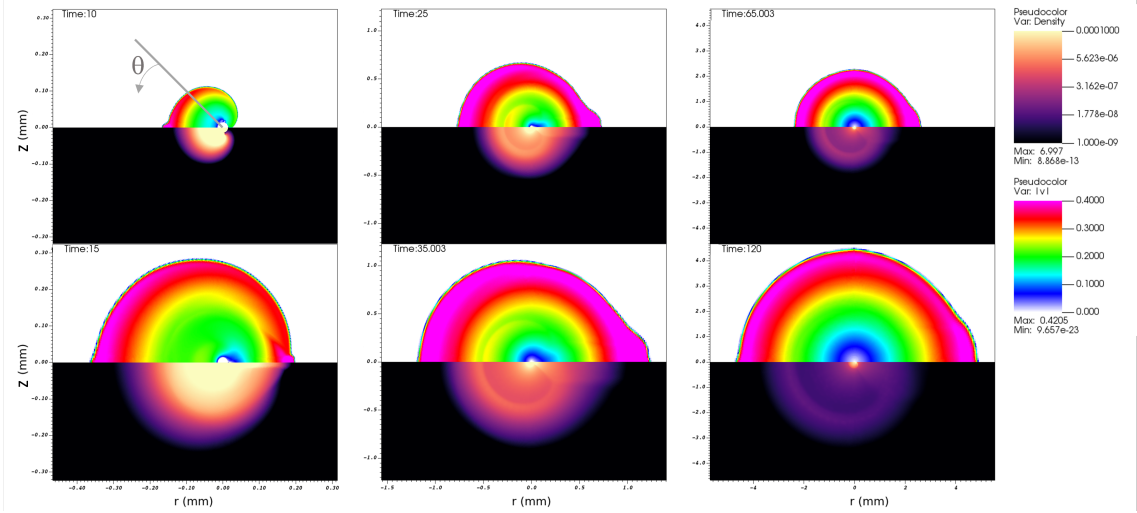
Figure 3.1: Six frames at times 10, 15, 25, 35, 65, and 120 ns of tin LPP expansion after illumination of the laser with laser energy of 8 mJ. Each panel shows 2D profiles of the plasma's speed ($|v|$ (10^5 ms^{-1})), at the top, and the density (cm^{-3}) at the bottom. In the t = 10 ns a gray line defines the emission angle. The laser approaches the tin droplet from $r = -\infty$ the left at z = 0 and $\theta = 0$.
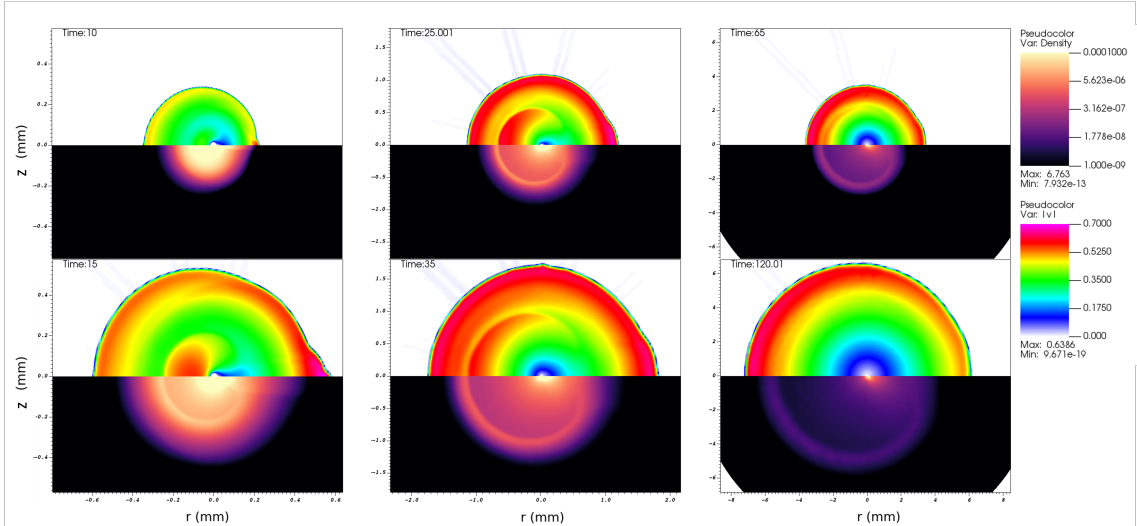

Figure 3.2: Six frames at times 10, 15, 25, 35, 65, and 120 ns of tin LPP expansion after illumination of the laser with laser energy of 97 mJ. Each panel shows 2D profiles of the ion speed ($|v|$ (10^5 ms^{-1})), at the top, and the ion density (cm^{-3}) at the bottom. The laser approaches the tin droplet from $r = -\infty$ the left at z = 0 and $\theta = 0$.

3.2 One-Dimensional Profile Speed and Density of Expanding LPP

In this section, we zoom in and quantify the results presented in the previous section. 1D profiles of velocity x_1 and density x_2 along lineouts (defined in the t = 10 ns panel in Fig 3.1) at five moments in time and for four different energies are presented in Fig 3.3. The emission angles, along which the lineouts are taken, at a 30°, 90°, and 120°angle are presented underneath each other in the figure. For all energies the first time-step is at t = 30 ns, when the LPP is no longer being illuminated by the laser pulse and the speed is in radial direction only. First, we observe in the velocity profiles that as the laser pulse energy increases, the velocity of the expanding plasma is also higher. Second, as shown in the frames of the expansion of the plasma in Fig 3.1 and 3.2, there is a second peak in velocity at a 30°emission angle. This is true for all E_L. However, the second burst is gaining in prominence as we look at higher laser pulse energies. At t = 30 ns the second peak for E = 8 mJ is just over half the value of the maximum velocity ($|v_{\max}|$), whereas for E = 97 the second burst reaches almost the same value as its $|v_{\max}|$. The second burst is most prominent in panel d_1 (E_L = 97 mJ and θ = 30°) and decreases in prominence at lower energy and for each energy at higher θ. Over time the second peak catches up, since the velocity is simply larger, with the first peak and the shape of the profile returns to a triangle-like shape as it turns into late-time behavior ($|v| \propto r/t$) of an explosion [30]. Lastly, the velocity profiles show that $|v_{\max}|$ is not constant over the expansion. At θ = 30°, this is not as significant, but at θ = 90°and θ = 120°, it is observed for all laser energies that the $|v_{\max}|$ is slightly decreasing over time. This is an effect of the non-perfect vacuum in the simulation, causing the outer part of the expanding LPP to slow down slightly. Another effect from the non-perfect vacuum is observed in the density profiles. Plateaus are showing around = 10^{-10} g cm^{-3}, this is also due to the background gas placed in the simulation. During the plasma expansion, the background gas is pushed outward and builds up just outside the plasma, causing these plateaus observed in the profiles. The density profiles $(x)_2$, show peaks at the small emission angle which turns to a less sharp peak as θ increases. This peak in density can be connected to the velocity of the plasma at the same distance $r_{\rho peak}$. Each peak in the density profiles matches the position ($r_{\rho peak}$)
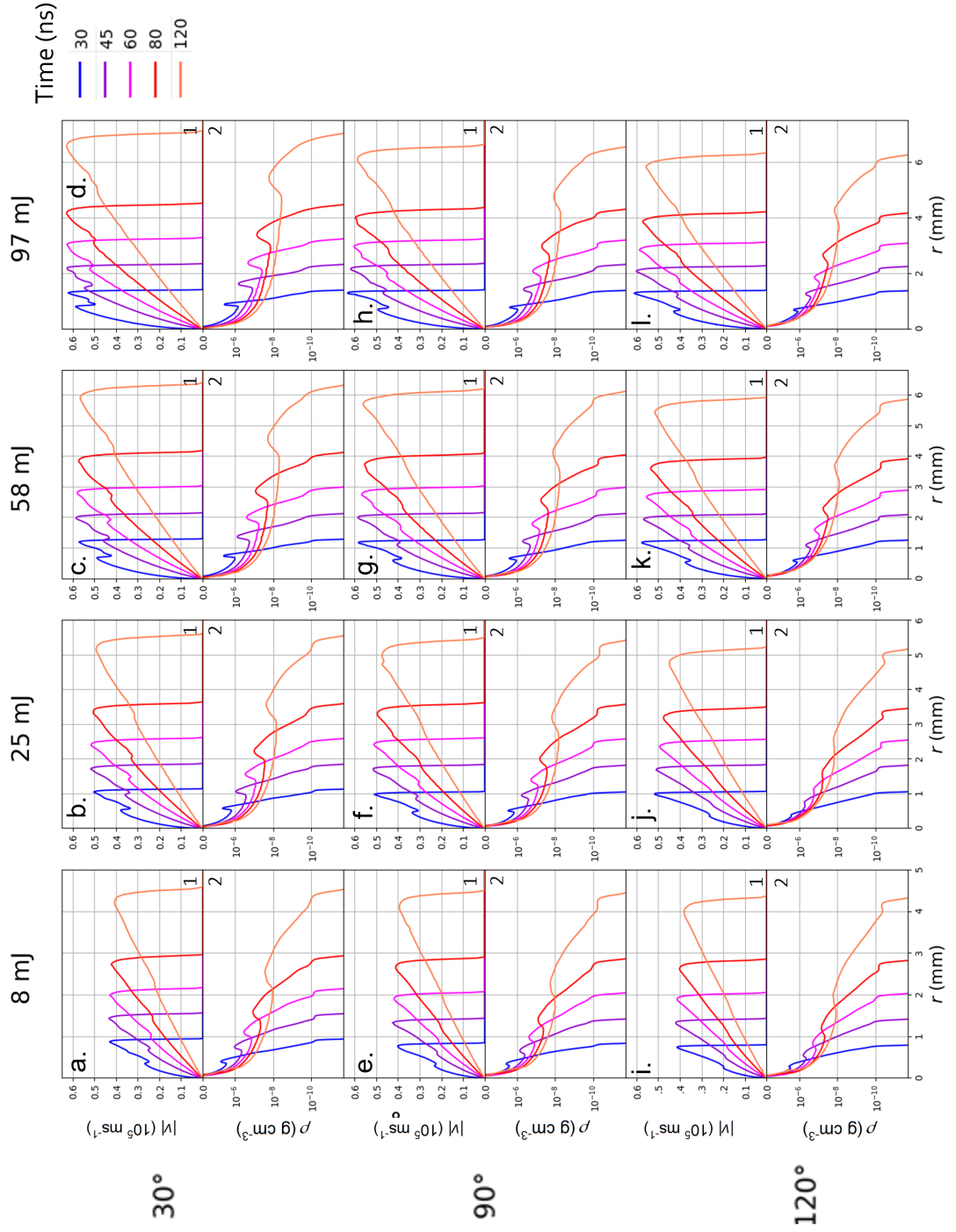
Figure 3.3: One-dimentional velocity (1) and density (2) profiles of lineouts along emission angles in front of (30°), above (90°) and behind (120°) the target. The latter is for four different laser energies. The lineouts are presented at t = 30, 45, 60, 80, and 120 ns after the laser incident on the droplet.

right after the second peak drops to the linearly shaped first peak. The latter could be a result of the faster moving at $r < r_{\rho peak}$ pushing the slower moving fluid outward, causing the density to rise. In all panels, it is also visible that the density plateaus right when the velocity starts to drop to zero. Here the most outer plasma is interacting with the background gas in the simulation, the collision with these slow-moving ions at the outer part of the expansion causes them to slightly build and thus show a plateau around $\rho = 10^{-10}$.

3.2.1 Speed of Expanding Plasma over Time

Here we shortly zoom in to the maximum velocity $|v_{\mathrm{max}}|$ of the plasma during the expansion. The first peak in the lineouts in Fig 3.3 seems to vary over
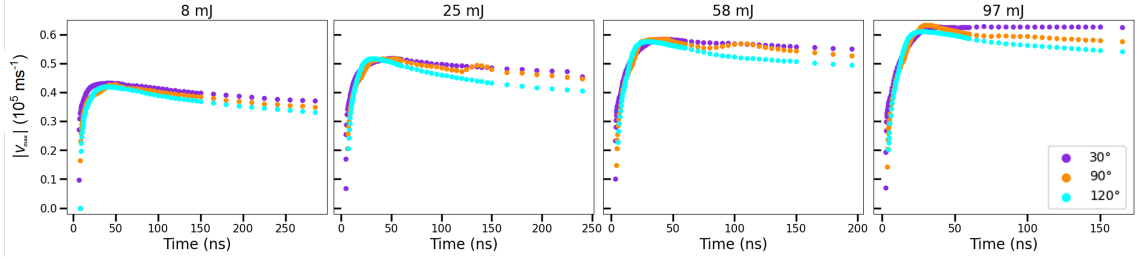

Figure 3.4: Maximum velocity ($|v_{\mathrm{max}}|$) of the expanding plasma plotted over time of four different energies at three angles, the front (30), the middle (90°), and the back (120°) of the target.

time at lower energies and higher emission angles. In all velocity panels $(x)_1$, except for panel $(d)_1$, the maximum velocity ($|v_{\mathrm{max}}|$) seems to decrease over time. To provide a clearer view of the $|v_{\mathrm{max}}|$, it is plotted over time for all four energies in Fig 3.4. The lowest and highest energies, 8 and 97 mJ, show that the velocity decreases faster as the emission angle increases. A 'bump' shows at the 90°emission angle for the pulse energies $E = 25$ mJ and $E = 58$ mJ, in the maximum velocity around $t = 100$ and $t = 150$ ns respectively. In the lineouts in Fig 3.3, panel f_1 (lineout at t = 80 ns) and g_1 (lineout at t = 60 ns) show a plateau forming around r = 2.5 mm. This plateau moves up towards the $|v_{\mathrm{max}}|$ (for E= 25 mJ and E = 58 mJ it is almost at $|v_{\mathrm{max}}|$ at t = 80 ns and t = 120 ns, respectively) until it blends in and gives the $|v_{\mathrm{max}}|$ an extra push. This is the cause for $|v_{\mathrm{max}}|$ increasing around t = 120 ns and t = 80 ns for the E = 25 mJ and E = 58 mJ panels, respectively, in Fig 3.4. Where this flow originates from, is not determined. However, it does not influence

the d^{2}N/dEdΩ distributions, see Fig 3.5, which will be discussed in the next section. What does trace back to these distributions is the velocity decreasing over angle. This causes the high-energy peak to shift to lower energy at larger angles.

3.3   Ion Energy Distributions

In this section, we present the ion energy distributions for the four different laser energies at seven different emission angles to analyze the anomalous high-energy peak that has been observed by the research group before.

In Fig 3.5 the experimentally (solid lines) obtained ion energy distributions
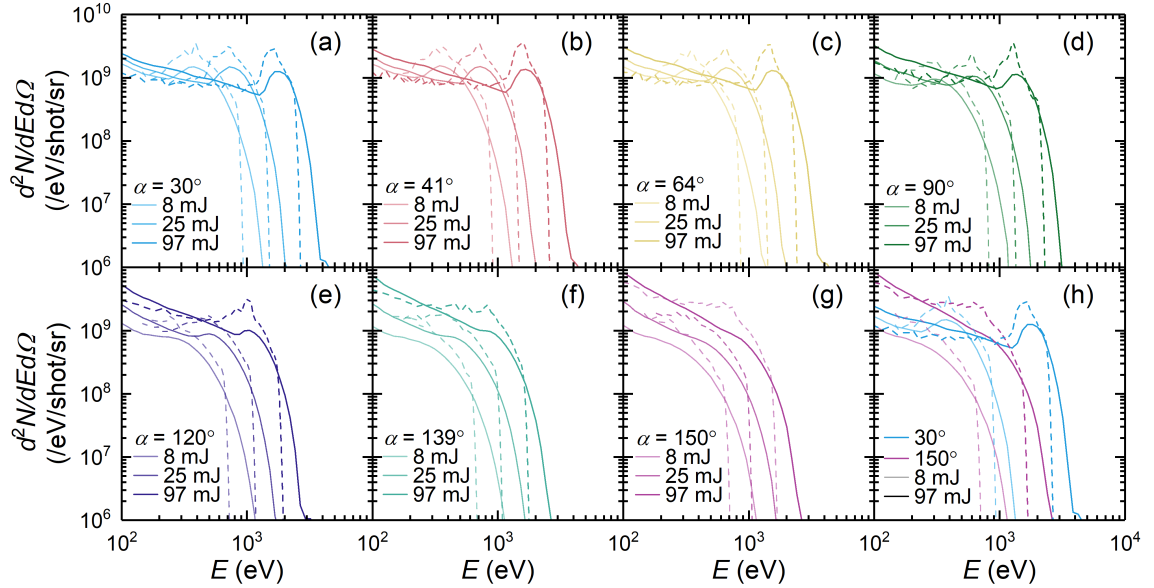
Figure 3.5: Experimentally (solid lines) and with simulations (dashed lines) obtained ion energy distributions at seven emission angles (panels a to g) and three laser energies. In panel h the lowest and highest energies are compared for the 30°and the 150°emission angle.

of four different laser energies are compared to the simulations (dashed lines). Seven emission angles are presented in panel a-g from the front of the target (θ = 30°) to the back of the target (θ = 150°). The data in this figure obtained with the simulations is averaged over a 10°window around the indicated angle and seems to be in good agreement with the experimentally obtained data. Unlike other models that describe plasma expansion (Murakami and Mora), the ion energy distributions show a high-energy peak, which is also observed in

the experiments. Thus agreeing well with the experiments.

In the distributions in front of the target (panel a-d) there is a high-energy peak observed in the distributions. As the laser energy decreases, this peak shifts to lower energy. These high-energy peaks are related to the peaks in the density lineouts discussed in the previous section. For each laser pulse energy it holds that where the density peaks, this area corresponds to a velocity that is directly related to the position of the peak as explained in more detail in [5]. Not only does the peak shift at lower energies, but also at larger emission angles the high-energy peak shifts to a lower value. The latter can be explained from the lineouts in Fig 3.3 and the changes in $|v_{\mathrm{max}}|$ shown in Fig 3.4. As already mentioned, the $|v_{\mathrm{max}}|$ of the plasma decreasing affects these ion energy distributions. When comparing E=97 mJ in panel a and d in Fig 3.5, the high-energy peak (in the simulation, dashed line) shifts from E $\approx$ 1660 eV to E $\approx$ 1100 eV, which is in direct relation to the velocity ($E = \frac{1}{2}mv^2$) $|v|$ $\propto r$ decreasing. The area wherein the density profiles peak, correlates with the velocity profiles right after the second burst. At this position, the velocity profiles afterward follow a linear shape to $|v_{\mathrm{max}}|$. As $|v_{\mathrm{max}}|$ decreases, which is directly related to the energy of the moving material $E = \frac{1}{2}mv^2$, the peak position energy also decreases.

The peak position is not the only thing that changes. Looking at the experimental data for E = 97 mJ, at higher emission angles the peaks become less and less prominent and cease to exist at $\theta > 140°$. The simulations also do not show a high-energy peak at larger emission angles. In panel e the 120°emission angle shows no peak for lower energies but does show a peak for the highest laser pulse energy.

In panel h of Fig 3.5, the highest and the lowest laser energy at the smallest and the largest emission angles are presented for comparison. For both laser energies, the high-energy peak is present at 30°and does not show at 150°. Also, at θ=150the ions have a lower maximum energy than the ions emitting to the front from the target.

3.3.1 Peak Position Relation to Laser Intensity

We want to determine whether simulations will be in agreement with experiments for other energies than the ones that are compared in this thesis. To do

so, we want to relate the high-energy peak in the energy distribution to laser intensity and see if this relation holds for the simulations. We do so by fitting a power law through the peak positions versus laser intensities, as expected in theory ($E_L \propto I^{0.7}$, Eq. 2.15). In Fig 3.6 the positions of the peaks are plotted against the four different intensities. The black dots and blue squares in panels (a) to (e) represent experiments and simulations respectively. The peak position is obtained by taking the maximum value in the distributions. Panel f presents the exponents B_α obtained from a power law fit ($A_\alpha I^{B_\alpha}$) at different emission angles (x-axis) are compared to the experimental and theoretically (Eq. 2.15) expected exponent (y-axis). Error bars here are results from the power law fit only, both for the experimental and simulated results. The fits result in an average value of $B_{\alpha,RAL} = 0.59$, where the exponent seems very stable over the different emission angles. This scaling relation shows very stable isotropic behavior over the emission angles which is not expected since the angular distributions show anisotropic spectra, as will be discussed in the following section.
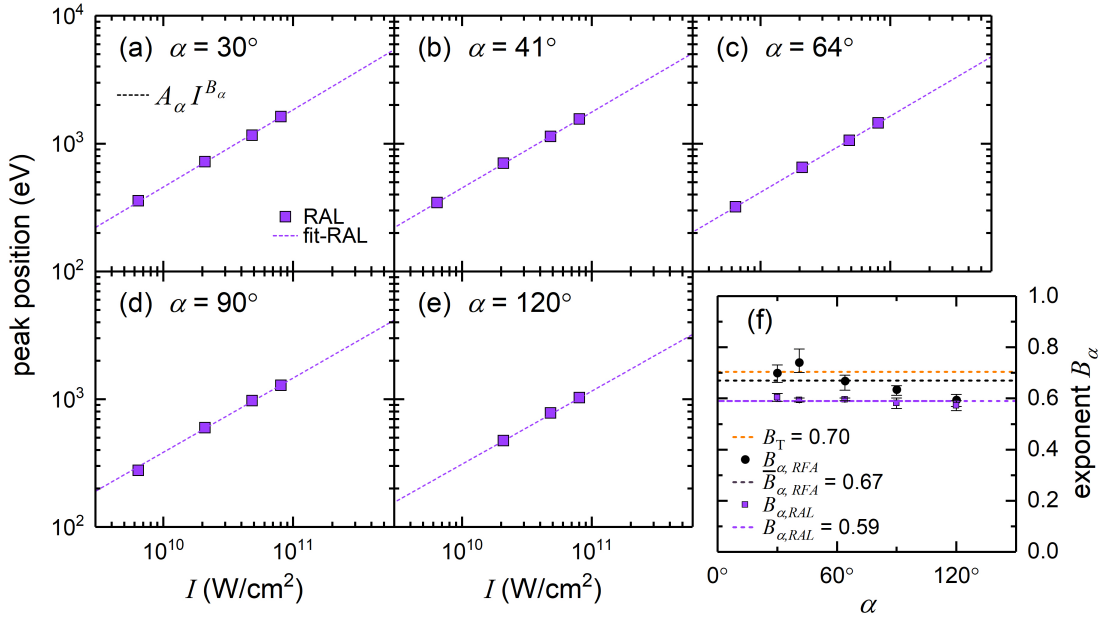

Figure 3.6: Positions of the high-energy peaks present in the ion energy distributions recorded by RALEF from panels a-e in Fig 3.5 are plotted against laser intensity. In panel f the exponent B_α obtained from a power law fit ($A_\alpha I^{B_\alpha}$) from different emission angles are compared to the experimental and theoretically (Eq. 2.15) expected exponent. The error bar corresponds to the standard deviation obtained from the fit, for both the experimental and simulated results.

3.4 Angular Distributions

To know how to surely protect the optics in the experiments, we want to know in what direction the plasma is expanding and what kinetic energy the emitted ions carry. In this section, the angular distributions of the total number of ions (obtained from the density profiles), the total energy and the total momentum of these ions in all emission angles are presented. Also, we discuss how the distributions differ over varying laser pulse energy.

Integrating the ion energy distributions gives an angular distribution of the amount of plasma flowing in a certain direction. From the energy distributions, the total energy emitted in a direction is obtained and thus also the total momentum of the expanding plasma. In [13], strong anisotropic behavior in the emission of tin ions is observed for a similar target incident by 60 mJ laser pulse Nd:YAG laser [13]. In Fig 3.7 from top to bottom: the angular distributions of the total number of ions, the total energy, and the total momentum are presented. Included is the expanded plasma with energies above 260 eV. This way we only take into consideration high-energy ions, which are most likely to damage the optics. In agreement with the experiments in [13] anisotropic behavior is observed in the simulated plasma expansion. The difference in energy cutoff - 60 eV in [13] and 260 eV in this thesis - has been studied and does not significantly influence the angular distributions with laser pulse energy $E = 97$ eV.

Also shown in Fig 3.7, in the right column, are the distributions normalized. Each is normalized by division by its own integral, making all integrals equal. The normalization enables a comparison of the shapes of the distributions. It seems that by reducing the laser energy, the angular distribution becomes more anisotropic. The lowers laser pulse energy has relatively higher energy plasma emitting to the front. Whereas when the laser energy increases, the distribution spreads out more to the back of the target. Since this is the result of single simulations for each laser pulse energy, the data is faltering. Averaging over multiple simulations and would smoothen the distributions.
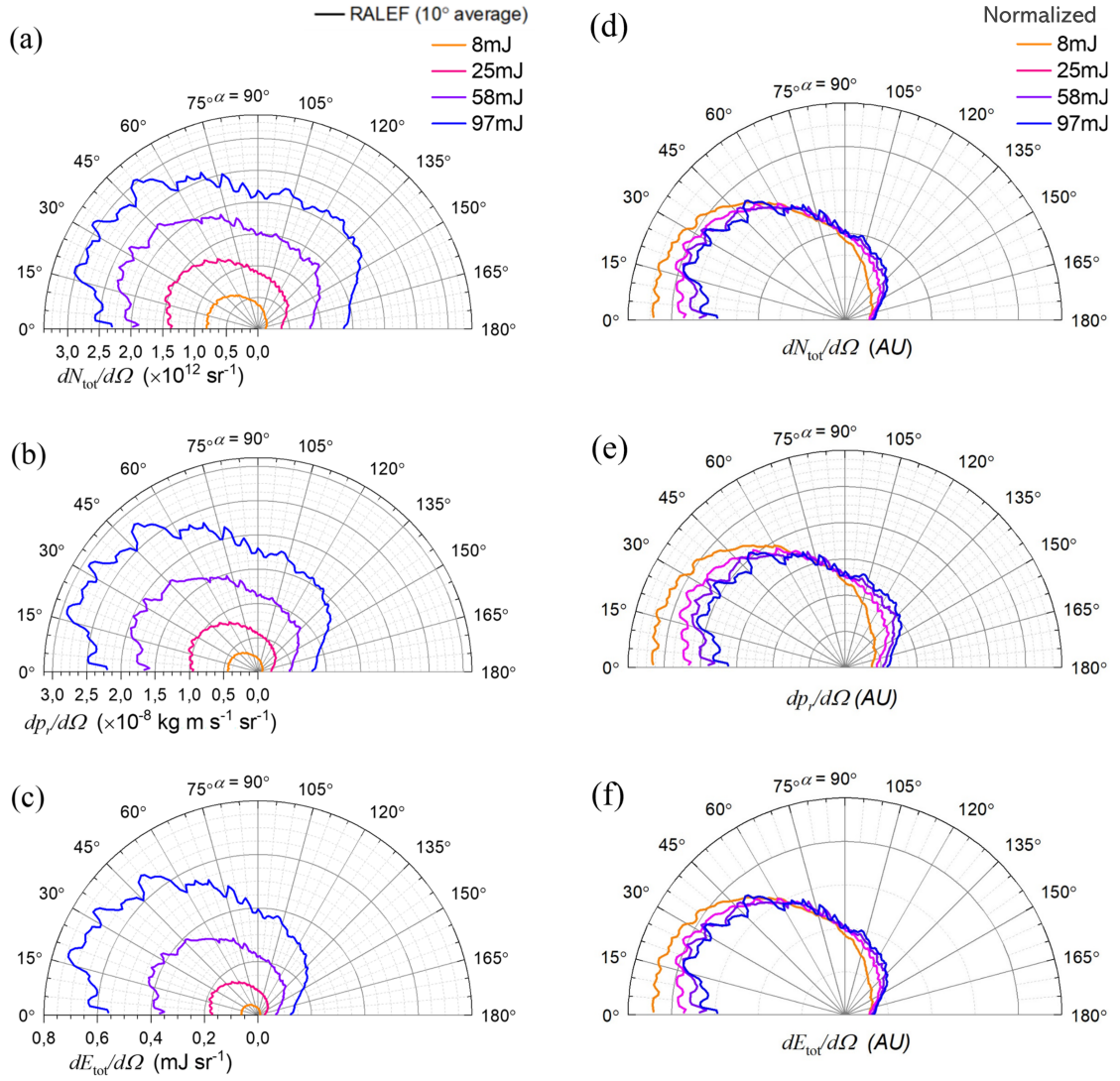
Figure 3.7: Angular distributions from four laser pulse energies are shown. From top to bottom: the total number of ions, the total momentum of the ions and the total energy of the ions emitted during the LPP expansion. The angular distributions have a running average of 10 degrees. In the right column, the angular distributions are normalized to compare the anisotropic behavior of the varying laser energies.

4

Conclusion

An understanding of the dynamics of laser-produced plasma that generates EUV is beneficial to the production of computer chips. To this end, we are interested in finding a model that faithfully describes a tin LPP expansion as observed in experiments, since such a model would allow us to predict how to properly protect the optics from ablating tin ions during the EUV generation process.

In this work, we investigate the abilities of the RALEF model using a single-fluid, single-temperature approach to simulate laser-produced plasma expansion arising from an Nd:YAG ($\lambda = 1.064 \ \mu$m) laser pulse irradiating a 27 μm diameter tin droplet. Using RALEF, LPP expansion has been simulated for four laser pulse energies between $5 - 100$ mJ.

In the experimental data, an anisotropy of the energy distribution is found. We show that the one-dimensional lineouts of the RALEF model also reproduce this anisotropy. The simulations enable tracking the velocity of the expanding fluid over time. The velocity at the front of the target ($\theta < 90°$) is - for all laser energies - higher than at the back of the target ($\theta > 90°$). With the direct relation between velocity and energy, this implies anisotropy in the expansion as is expected from the experimentally obtained ion energy distributions.

For simulations of the four laser pulse energies that are performed, RALEF records ion energy distributions that agree with the experiment. Notably, the simulation reveals ion energy distributions featuring a high-energy peak in agreement - both in terms of energy and spectral intensity - with the peak observed in the experimental data. The high energy peak in the numerically

reproduced ion energy distributions follows a power law relation with the irradiating laser intensity. This power law exponent shows that the relation between peak position and laser intensity is similar to the relation between sonic speed energy in plasma and laser intensity. The power law exponent found using the simulations matches well with both experimentally obtained results and theoretical studies. Interestingly, the power law exponent shows isotropic behavior, even though the energy distributions are clearly anisotropic for all intensities. Thus, from this, it can be concluded that when a peak in the ion energy distributions is present the high-energy peak position follows the power law scaling. In conclusion, we successfully simulate tin laser-produced plasma expansion using the RALEF code, replicating the anisotropic ion energy distributions observed in experiments. We demonstrate the power-law scaling of the high-energy peak position. These findings validate that the single-fluid, single-temperature approach suffices for the purpose of modeling these expansions. This ability to predict the LPP expansion dynamics faithfully may be leveraged to gain valuable insights into safeguarding optics during EUV light generation, benefiting the production of computer chips.

5

Acknowledgements

References

[1] O. O. VERSOLATO, J. SHEIL, S. WITTE, W. UBACHS, AND R. HOEK-
STRA. **Microdroplet-tin plasma sources of EUV radiation driven
by solid-state-lasers (Topical Review)**, 5 2022.

[2] P. MORA. **Plasma Expansion into a Vacuum**. *Physical Review Letters*,
90:4, 2003.

[3] IAKOV BORISOVICH ZELDOVICH, YURII PETROVICH RAIZER, AND WAL-
LACE D HAYES. *Physics of shock waves and high-temperature hydrody-
namic phenomena*, **1**. Academic Press New York, 1966.

[4] M. MURAKAMI, Y. G. KANG, K. NISHIHARA, S. FUJIOKA, AND
H. NISHIMURA. **Ion energy spectrum of expanding laser-plasma
with limited mass**. *Physics of Plasmas*, **12**:1–8, 2005.

[5] D. J. HEMMINGA, L. POIRIER, M. M. BASKO, R. HOEKSTRA,
W. UBACHS, O. O. VERSOLATO, AND J. SHEIL. **High-energy ions
from Nd:YAG laser ablation of tin microdroplets: Compari-
son between experiment and a single-fluid hydrodynamic model**.
Plasma Sources Science and Technology, **30**, 10 2021.

[6] SASˇA BAJT. **Improved reflectance and stability of Mo-Si multi-
layers**. *Optical Engineering*, **41**:1797, 8 2002.

[7] SS HARILAL, BEAU O'SHAY, AND MARK S TILLACK. **Debris mitiga-
tion in a laser-produced tin plume using a magnetic field**. *Journal
of applied physics*, **98**(3), 2005.

[8] D. B. ABRAMENKO, M. V. SPIRIDONOV, P. V. KRAINOV, V. M.
KRIVTSUN, D. I. ASTAKHOV, V. V. MEDVEDEV, M. VAN KAMPEN,

D. Smeets, and K. N. Koshelev. **Measurements of hydrogen gas stopping efficiency for tin ions from laser-produced plasma**. *Applied Physics Letters*, **112**, 4 2018.

[9] H Mizoguchi et al. **Extreme Ultraviolet (EUV) Lithography XI vol 11323 ed NM Felix**. *A Lio (Bellingham, WA: International Society for Optics and Photonics (SPIE)) pp*, pages 225–38, 2020.

[10] Igor Fomenkov, David Brandt, Alex Ershov, Alexander Schafgans, Yezheng Tao, Georgiy Vaschenko, Slava Rokitski, Michael Kats, Michael Vargas, Michael Purvis, Rob Rafac, Bruno La Fontaine, Silvia De Dea, Andrew LaForge, Jayson Stewart, Steven Chang, Matthew Graham, Daniel Riggs, Ted Taylor, Mathew Abraham, and Daniel Brown. **Light sources for high-volume manufacturing EUV lithography: Technology, performance, and power scaling**, 6 2017.

[11] Daisuke Nakamura, Koji Tamaru, Yuki Hashimoto, Tatsuo Okada, Hiroki Tanaka, and Akihiko Takahashi. **Mitigation of fast ions generated from laser-produced Sn plasma for extreme ultraviolet light source by H2 gas**. *Journal of Applied Physics*, **102**, 2007.

[12] Shinsuke Fujioka, Hiroaki Nishimura, Katsunobu Nishihara, Masakatsu Murakami, Youngces G. Kang, Qincui Gu, Keiji Nagai, Takayoshi Norimatsu, Noriaki Miyanaga, Yasukazu Izawa, Kunioki Mima, Yoshinori Shimada, Atsushi Sunahara, and Hiroyuki Furukawa. **Properties of ion debris emitted from laser-produced mass-limited tin plasmas for extreme ultraviolet light source applications**. *Applied Physics Letters*, **87**:1–3, 2005.

[13] Lucas Poirier, Diko J Hemminga, Adam Lassise, Luc Assink, Ronnie Hoekstra, John Sheil, and Oscar O Versolato. **Strongly anisotropic ion emission in the expansion of Nd: YAG-laser-produced plasma**. *Physics of Plasmas*, **29**(12):123102, 2022.

[14] ANDREA MACCHI, MARCO BORGHESI, AND MATTEO PASSONI. **Ion acceleration by superintense laser-plasma interaction**. *Reviews of Modern Physics*, **85**:751–793, 5 2013.

[15] R. A. MEIJER, D. KURILOVICH, B. LIU, Z. MAZZOTTA, J. HERNANDEZ-RUEDA, O. O. VERSOLATO, AND S. WITTE. **Nanosecond laser ablation threshold of liquid tin microdroplets**. *Applied Physics A: Materials Science and Processing*, **128**, 7 2022.

[16] AKIRA SASAKI, ATSUSHI SUNAHARA, HIROYUKI FURUKAWA, KATSUNOBU NISHIHARA, SHINSUKE FUJIOKA, TAKESHI NISHIKAWA, FUMIHIRO KOIKE, HAYATO OHASNI, AND HAJIME TANUMA. **Modeling of radiative properties of Sn plasmas for extreme-ultraviolet source**. *Journal of Applied Physics*, **107**, 6 2010.

[17] S. S. CHURILOV AND A. N. RYABTSEV. **Analysis of the spectra of in XII-XIV and Sn XIII-XV in the far-VUV region**. *Optics and Spectroscopy (English translation of Optika i Spektroskopiya)*, **101**:169–178, 8 2006.

[18] J. COLGAN, D. P. KILCREASE, J. ABDALLAH, M. E. SHERRILL, C. J. FONTES, P. HAKEL, AND G. S.J. ARMSTRONG. **Atomic structure considerations for the low-temperature opacity of Sn**. *High Energy Density Physics*, **23**:133–137, 6 2017.

[19] J. SCHEERS, J. SCHEERS, C. SHAH, A. RYABTSEV, H. BEKKER, F. TORRETTI, F. TORRETTI, J. SHEIL, D. A. CZAPSKI, J. C. BERENGUT, W. UBACHS, W. UBACHS, J. R.CRESPO LÓPEZ-URRUTIA, R. HOEKSTRA, R. HOEKSTRA, AND O. O. VERSOLATO. **EUV spectroscopy of highly charged Sn13+-Sn15+ ions in an electron-beam ion trap**. *Physical Review A*, **101**, 6 2020.

[20] F. TORRETTI, J. SHEIL, R. SCHUPP, M. M. BASKO, M. BAYRAKTAR, R. A. MEIJER, S. WITTE, W. UBACHS, R. HOEKSTRA, O. O. VERSOLATO, A. J. NEUKIRCH, AND J. COLGAN. **Prominent radiative contributions from multiply-excited states in laser-produced tin plasma for nanolithography**. *Nature Communications*, **11**, 12 2020.

[21] F. Gobet, M. Comet, J. R. Marquès, V. Méot, X. Raymond, M. Versteegen, J. L. Henares, and O. Morice. **Signatures of fluid and kinetic properties in the energy distributions of multicharged Ta ions from nanosecond-laser-heated plasma**. *Physical Review E*, **98**, 12 2018.

[22] M. M. Basko, V. G. Novikov, and A. S. Grushin. **On the structure of quasi-stationary laser ablation fronts in strongly radiating plasmas**. *Physics of Plasmas*, **22**, 5 2015.

[23] Katsunobu Nishihara, Atsushi Sunahara, Akira Sasaki, Masanori Nunami, Hajime Tanuma, Shinsuke Fujioka, Yoshinori Shimada, Kazumi Fujima, Hiroyuki Furukawa, Takako Kato, et al. **Plasma physics and radiation hydrodynamics in developing an extreme ultraviolet light source for lithography**. *Physics of Plasmas*, **15**(5), 2008.

[24] M Murakami and MM Basko. **Self-similar expansion of finite-size non-quasi-neutral plasmas into vacuum: Relation to the problem of ion acceleration**. *Physics of plasmas*, **13**(1), 2006.

[25] A. Sunahara and K. A. Tanaka. **Atomic number Z dependence of dynamics of laser-ablated materials**. **85**, pages 935–939, 11 2010.

[26] Frank L Addessio, John R Baumgardner, John K Dukowicz, Norman L Johnson, Bryan A Kashiwa, Rick M Rauenzahn, and Charles Zemach. **CAVEAT: A computer code for fluid dynamics problems with large distortion and internal slip. Revision 1**. Technical report, Los Alamos National Lab.(LANL), Los Alamos, NM (United States), 1992.

[27] M. M. Basko. **On the maximum conversion efficiency into the 13.5-nm extreme ultraviolet emission under a steady-state laser ablation of tin microspheres**. *Physics of Plasmas*, **23**, 8 2016.

[28] M. M. Basko, M. S. Krivokorytov, A. Yu Vinokhodov, Yu V. Sidelnikov, V. M. Krivtsun, V. V. Medvedev, D. A. Kim, V. O. Kompanets, A. A. Lash, and K. N. Koshelev. **Fragmentation**

dynamics of liquid-metal droplets under ultra-short laser pulses. *Laser Physics Letters*, **14**, 3 2017.

[29] DMITRY KURILOVICH, MIKHAIL M. BASKO, DMITRII A. KIM, FRANCESCO TORRETTI, RUBEN SCHUPP, JIM C. VISSCHERS, JORIS SCHEERS, RONNIE HOEKSTRA, WIM UBACHS, AND OSCAR O. VERSOLATO. **Power-law scaling of plasma pressure on laser-ablated tin microdroplets**. *Physics of Plasmas*, **25**, 1 2018.

[30] YA B ZEL'DOVICH AND YU P RAIZER. *Physics of shock waves and high-temperature hydrodynamic phenomena*. Courier Corporation, 2002.